

Solving the Ghost-Gluon System of Yang-Mills Theory on GPUs

Markus Hopfer^{a,*}, Reinhard Alkofer^a, Gundolf Haase^b

^a*Institut für Physik, Karl-Franzens Universität, Universitätsplatz 5, 8010 Graz, Austria*

^b*Institut für Mathematik und wissenschaftliches Rechnen, Karl-Franzens Universität, Heinrichstraße 36, 8010 Graz, Austria*

Abstract

We solve the ghost-gluon system of Yang-Mills theory using Graphics Processing Units (GPUs). Working in Landau gauge, we use the Dyson-Schwinger formalism for the mathematical description as this approach is well-suited to directly benefit from the computing power of the GPUs. With the help of a Chebyshev expansion for the dressing functions and a subsequent appliance of a Newton-Raphson method, the non-linear system of coupled integral equations is linearized. The resulting Newton matrix is generated in parallel using OpenMPI and CUDATM. Our results show, that it is possible to cut down the run time by two orders of magnitude as compared to a sequential version of the code. This makes the proposed techniques well-suited for Dyson-Schwinger calculations on more complicated systems where the Yang-Mills sector of QCD serves as a starting point. In addition, the computation of Schwinger functions using GPU devices is studied.

Keywords: Ghost-Gluon System, Yang-Mills, Dyson-Schwinger equations, parallel computing, CUDATM programming model, Graphics Processing Units

1. Introduction

It is well-established by now that quantum chromodynamics (QCD) provides the necessary framework to describe the strong interaction among quarks and gluons. It is furthermore believed that confinement, which denotes the absence of color charged objects from the physical spectrum, origins from the gauge sector of the theory. Here, the infrared properties of the one-particle irreducible Green's functions are of particular interest. Due to the large value of the coupling in this low-energy regime, a non-perturbative treatment is mandatory. The Dyson-Schwinger (or generally a Green's functions) approach provides a continuum formulation of QCD [1–5] capable to describe the system over the entire momentum range. Dyson-Schwinger equations (DSEs) constitute a highly coupled system of non-linear integral equations, the equations of motion for the underlying quantum field theory. If there were the possibility to solve these equations self-consistently, the whole

*corresponding author

Email addresses: `markus.hopfer@uni-graz.at` (Markus Hopfer), `reinhard.alkofer@uni-graz.at` (Reinhard Alkofer), `gundolf.haase@uni-graz.at` (Gundolf Haase)

dynamics of the quantum system would be uncovered [6]. Unfortunately, each DSE comprehends higher order Green's functions, such that the whole system builds up to an infinite tower of n -point functions and an appropriate truncation is mandatory. The truncation procedure is a highly non-trivial task and one has to account for errors induced by the particular truncation scheme. On the other hand, and based on the work of [7–9], there has also been substantial progress in solving the whole tower in the far infrared [10–12].

Initiated by Mandelstam [13] the gluon propagator and later the ghost-gluon system was at the focus of many contemporary DSE studies. Recent investigations agree on an enhancement of the ghost whereas the gluon propagator is suppressed in the infrared regime [14–19]. This picture is also enforced by results obtained from lattice simulations, see, *e.g.*, [20, 21] and references therein, or Functional Renormalization Group methods [22]. Whether or not the gluon propagator exactly vanishes in the infrared has been discussed for quite some time ¹. Although this so-called scaling solution is predicted by continuum approaches it is, in four space-time dimensions, not seen in recent lattice calculations of the gluon propagator [21], see however [27–29].

Within the last years, Graphics Processing Units (GPUs) became an essential branch in high performance computing. Their efficiency, *i.e.* the ratio between computational power and power consumption, makes them a reasonable alternative to conventional clusters. With the availability of low-cost consumer GPU devices this technology also finds its way into desktop computers offering the possibility to perform general purpose scientific and engineering computations in an until then not feasible way. However, the mapping of existing algorithms and/or software to the massively parallel SIMD architecture of the GPU is often difficult such that a restructuring of the algorithms/code is inevitable in order to meet the requirements of the hardware. In case of the ghost-gluon system only minimal modifications are needed such that the portation of the sequential code is a straightforward task. The main objective of this paper is to employ the benefits of modern GPU devices into DSE calculations. Here, Yang-Mills theory is not only an interesting topic on its own but serves also as a starting point for investigations involving fermions since the treatment of larger systems by incorporating additional DSEs is possible with the proposed methods. Compared to the sequential code, performance gains by two orders of magnitude can be obtained. This paper is organized as follows. In Section 2 we introduce the mathematical formulation of the problem. In Section 3 a description of the employed numerical methods will be given, where the parallelization will be detailed in Section 4. Finally in Section 5 we compare the performance of the sequential code with the parallelized versions using CUDATM as well as OpenMPI and, in addition, the computation of Schwinger functions on GPU devices will be outlined. Our summary and conclusions will be given in Section 6.

¹This would correspond to an infrared singular ghost propagator, *i.e.*, a scenario in accordance with the Kugo-Ojima [23, 24] and Gribov-Zwanziger [25, 26] confinement criterion.

2. The Dyson-Schwinger Equations for the Ghost-Gluon System

Within the DSE approach to QCD the Yang-Mills system is described by a set of coupled integral equations for the corresponding ghost and gluon propagator as depicted in Figs. 1-2, where throughout this paper Landau gauge is used. Note that the DSE for the gluon propagator is already truncated in order to render the system tractable². Thus, no two-loop as well as no tadpole diagrams are taken into account. The black dots indicate dressed propagators whereas the blue blobs represent dressed vertices.

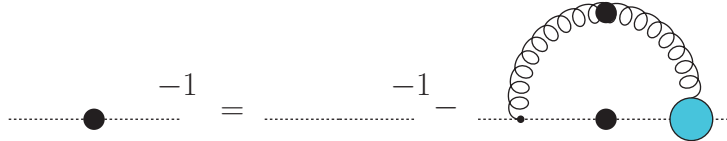


Figure 1: The DSE for the Landau gauge ghost propagator.

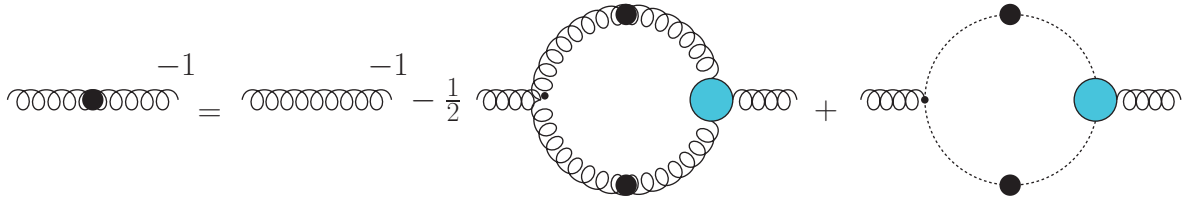


Figure 2: The truncated DSE for the Landau gauge gluon propagator.

The corresponding formal expression for the ghost propagator reads

$$D_G^{-1}(p) = \tilde{Z}_3 D_{G,0}^{-1}(p) - \tilde{Z}_1 g^2 N_c \int \frac{d^4 q}{(2\pi)^4} \Gamma_{\mu,0}(p, q) D_{\mu\nu}(p - q) \Gamma_\nu(q, p) D_G(q), \quad (1)$$

where for the gluon propagator it is given by

$$D_{\mu\nu}^{-1}(p) = Z_3 D_{\mu\nu,0}^{-1}(p) + \tilde{Z}_1 g^2 N_c \int \frac{d^4 q}{(2\pi)^4} \Gamma_{\mu,0}(p, q) D_G(p - q) \Gamma_\nu(q, p) D_G(q) - Z_1 g^2 \frac{N_c}{2} \int \frac{d^4 q}{(2\pi)^4} \Gamma_{\mu\rho\sigma,0}(p, q) D_{\rho\rho'}(p - q) \Gamma_{\rho'\nu\sigma'}(q, p) D_{\sigma\sigma'}(q). \quad (2)$$

Here, D/Γ denotes the dressed and bare propagators/vertices respectively. N_c is the number of colors and \tilde{Z}_1 is the renormalization constant for the ghost-gluon vertex which can be set to one in Landau gauge as this vertex is UV finite [30]. Furthermore, Z_1 is the renormalization constant for the three-gluon vertex and \tilde{Z}_3 and Z_3 denote the wave-function renormalization constants for the ghost and gluon, respectively. For the purpose of this

²Throughout this section the notation is adapted from [16] where this system has been solved.

numerical study it is sufficient to replace the dressed ghost-gluon vertex by its bare counterpart, i.e. $\Gamma_\nu(q, p) = iq_\nu$, whereas for the three-gluon vertex the model proposed in [16] is employed

$$\Gamma_{\mu\nu\sigma}(q, p) = \frac{1}{Z_1} \frac{G(q^2)^{1-a/\delta-2a}}{Z(q^2)^{1+a}} \frac{G(k^2)^{1-b/\delta-2b}}{Z(k^2)^{1+b}} \Gamma_{\mu\nu\sigma,0}(q, p), \quad (3)$$

with $k^2 \equiv (q-p)^2$. The choice of $a = b = 3\delta$, where $\delta = -9/44$ is the anomalous dimension of the ghost, leads to the correct scaling of the dressing functions in the ultraviolet region³. Using $O(4)$ invariance in the Euclidean formulation of QCD, the four dimensional integrals can be rewritten in the form

$$\int d^4q = 4\pi \int_0^{\Lambda^2} dy \frac{y}{2} \int_0^\pi d\theta \sin^2 \theta, \quad (4)$$

where two integrations are carried out trivially yielding a factor of 4π . Here we introduced the abbreviation $q^2 = y$ for the loop momentum⁴. In the following we furthermore use $p^2 = x$ and $k^2 = z$. For the radial integral we employ a standard *Gauss-Legendre quadrature* rule, where the nodes are appropriately distributed over the whole momentum range by using a non-linear mapping function. For the angular integration we use a *tanh-sinh quadrature* [31] as the integral can be rewritten as

$$\int_0^\pi d\theta \sin^2 \theta \rightarrow \int_{-1}^1 d\xi \sqrt{1-\xi^2}, \quad (5)$$

with $\xi \equiv \cos \theta$. This quadrature rule is well-suited for the occurring integrands, showing singular behavior at the boundaries of the integration region. Compared to a *Gauss-Chebyshev quadrature* we need much less integration points to get the same - if not better - results for the angular integration. With the following ansatz for the ghost propagator

$$D_G(p) = -\frac{G(p^2)}{p^2} \quad (6)$$

as well as for the gluon propagator

$$D_{\mu\nu}(p) = \left(\delta_{\mu\nu} - \frac{p_\mu p_\nu}{p^2} \right) \frac{Z(p^2)}{p^2}, \quad (7)$$

the corresponding DSEs can be rewritten

$$G(x)^{-1} = \tilde{Z}_3 - \frac{g^2 N_c}{(2\pi)^3} \int_0^{\Lambda^2} dy y G(y) \int_{-1}^1 d\xi (1-\xi)^{3/2} \frac{Z(z)}{z^2}, \quad (8)$$

$$\begin{aligned} Z(x)^{-1} &= Z_3 + \frac{g^2 N_c}{(2\pi)^3} \frac{1}{3x} \int_0^{\Lambda^2} dy \int_{-1}^1 d\xi (1-\xi^2)^{1/2} Q(x, y, z) \frac{(G(y)G(z))^{-2-6\delta}}{(Z(y)Z(z))^{3\delta}} \\ &+ \frac{g^2 N_c}{(2\pi)^3} \frac{1}{3x} \int_0^{\Lambda^2} dy \int_{-1}^1 d\xi (1-\xi^2)^{1/2} M(x, y, z) G(y)G(z), \end{aligned} \quad (9)$$

³For small momenta, the model approaches a constant value, which is reasonable as the gluon loop diagram is sub-leading the infrared regime.

⁴We regularized the system using a sharp momentum cutoff Λ^2 .

where the integral kernels read⁵

$$M(x, y, z) = \frac{1}{z} \left(-\frac{1}{4}x + \frac{y}{2} - \frac{1}{4} \frac{y^2}{x} \right) + \frac{1}{2} + \frac{1}{2} \frac{y}{x} - \frac{1}{4} \frac{z}{x}, \quad (10)$$

$$\begin{aligned} Q(x, y, z) &= \frac{1}{z^2} \left(\frac{1}{8} \frac{x^3}{y} + x^2 - \frac{9}{4}xy + y^2 + \frac{1}{8} \frac{y^3}{x} \right) \\ &+ \frac{1}{z} \left(\frac{x^2}{y} - 4(x+y) + \frac{y^2}{x} \right) - \left(\frac{9}{4} \frac{x}{y} + 4 + \frac{9}{4} \frac{y}{x} \right) \\ &+ z \left(\frac{1}{x} + \frac{1}{y} \right) + z^2 \frac{1}{8xy} + \frac{15}{4}. \end{aligned} \quad (11)$$

To introduce a convenient notation the above equations are rewritten

$$G(x)^{-1} = \tilde{Z}_3 + \Pi_G(x), \quad (12)$$

$$Z(x)^{-1} = Z_3 + \Pi_Z(x), \quad (13)$$

and a MOM scheme is applied in the next step

$$G(x)^{-1} = G(x_G)^{-1} + \Pi_G(x) - \Pi_G(x_G) \quad (14)$$

$$Z(x)^{-1} = Z(x_Z)^{-1} + \Pi_Z(x) - \Pi_Z(x_Z). \quad (15)$$

In this renormalization scheme we subtract the equations at some squared momenta x_G and x_Z , treating $G(x_G)^{-1}$ and $Z(x_Z)^{-1}$ as new parameters to fix the system. Furthermore, in the limits of very small/large external momenta x the system can be solved analytically, where in the infrared region one finds⁶

$$Z(x \ll 1) = A x^{2\kappa}, \quad (16)$$

$$G(x \ll 1) = B x^{-\kappa}, \quad (17)$$

with $\kappa \approx 0.595353$ and some general coefficients A and B . These two coefficients are fixed by demanding that the analytical solution must coincide with the numerical solution at a specific matching point ϵ^2 in the infrared regime. Similar to this, one can apply a logarithmic ansatz for the dressing functions in the ultraviolet region

$$G(x \gg 1) = G_{UV} \left[\omega \ln \left(\frac{x}{x_{UV}} \right) + 1 \right]^\delta \quad (18)$$

$$Z(x \gg 1) = Z_{UV} \left[\omega \ln \left(\frac{x}{x_{UV}} \right) + 1 \right]^\gamma. \quad (19)$$

⁵In the last line an additional term $15/4$ is added in order to cancel spurious quadratic divergencies introduced by the truncation. These divergencies would be absent in a full treatment. A pragmatic approach is to remove them by hand by adding an additional term. Furthermore, in the numerical implementation we optimized the kernels to avoid unnecessary division operations.

⁶See Ref. [16] for a detailed analysis of the IR/UV behavior of the dressing functions.

The analytical treatment yields $\omega = 11N_c\alpha(\mu^2)/12\pi$, where $\alpha(\mu^2) = g^2/4\pi$ is the coupling at the renormalization scale μ . The constants G_{UV} and Z_{UV} are fixed by matching the numerical solutions at $x_{UV} = \Lambda^2$ and $\gamma = -13/22$ is the anomalous dimension of the gluon. To allow to put in the following sections the focus on the numerical methods only we will present the numerical results for the dressing functions, the running coupling and the Schwinger functions already here.

2.1. Dressing Functions and Running Coupling

With an appropriate choice of $G(x_G)$ and $Z(x_Z)$ the system is fixed, where we use $x_G = 0$ and $x_Z = \Lambda^2 = 5 \times 10^4 \text{ GeV}^2$ in our calculations. In Fig. 3 the ghost and gluon dressing function is plotted, where $Z(x_Z) = 0.256$ and $\alpha(\mu^2) = 1$ is used⁷.

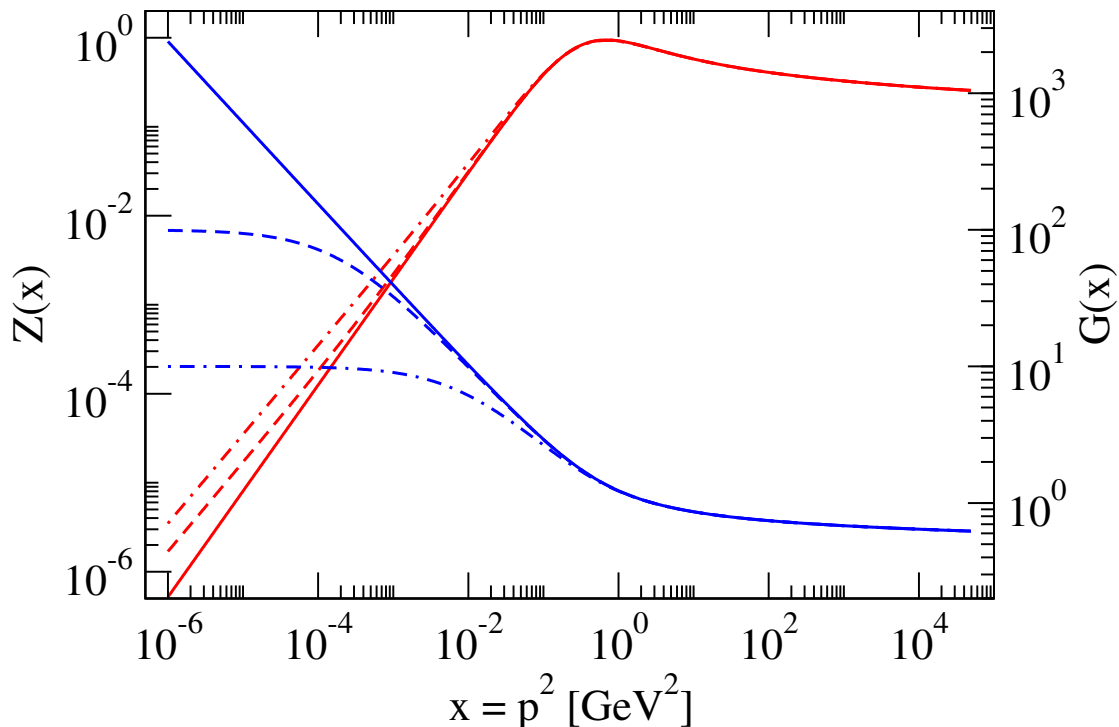


Figure 3: The scaling solution (solid line) as well as two decoupling solutions (dashed lines) for the ghost and gluon propagator on a $\log - \log$ plot. For the latter case, we used $G(x_G)^{-1} = 0.01$ (dashed line) and $G(x_G)^{-1} = 0.1$ (dashed-dotted line).

The choice of $G(x_G)^{-1} = 0$ leads to an infrared singular ghost dressing function, whereas the corresponding gluon dressing function vanishes in this regime. This is the so-called *scaling solution*. A non-vanishing value of $G(x_G)^{-1} > 0$ yields a *decoupling solution* which

⁷Note that these values are arbitrary in principle. Although, together with our choice for $\alpha(\mu^2)$ they yield the correct experimental value $\alpha(M_Z^2) = 0.118$ for the running coupling, where $M_Z = 91.2 \text{ GeV}$ is the Z-boson mass. The renormalization scale μ is implicitly fixed by specifying a value for $\alpha(\mu^2)$, where the renormalization condition $G^2(\mu^2)Z(\mu^2) = 1$ is used.

is indicated by the dashed/dashed-dotted lines. In Fig. 4 the non-perturbative running coupling $\alpha(x) = \alpha(\mu^2)G^2(x)Z(x)$ is plotted.

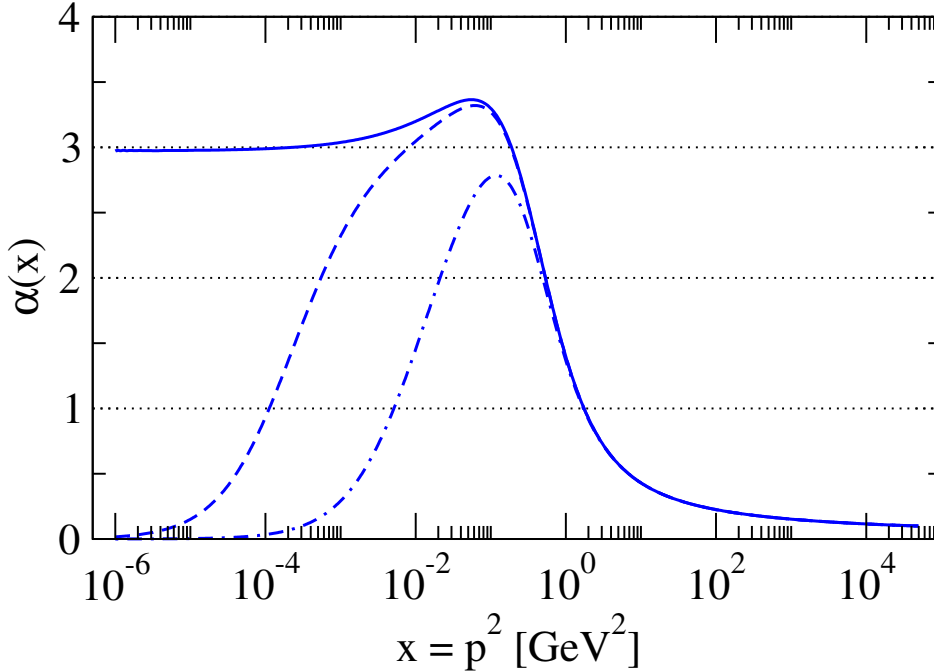


Figure 4: The non-perturbative running coupling $\alpha(x)$ on a *log-linear* plot. The scaling solution (solid line) is compared to the decoupling solution, where in the latter case $G(x_G)^{-1} = 0.01$ (dashed line) and $G(x_G)^{-1} = 0.1$ (dashed-dotted line) is used.

The infrared fixed point is $\alpha(0) \approx 8.915/N_C = 2.972$ in the scaling case. In the decoupling case the running coupling vanishes in the infrared region which agrees with DSE calculations on a compact manifold [32] and lattice calculations [33].

2.2. Schwinger Functions

Schwinger functions are a helpful tool when exploring the analytic structure of propagators. Although a detailed description is beyond the scope of this paper⁸ we want to note the following: Within the Euclidean formulation of quantum field theory, negative norm contributions to a specific propagator correspond to a violation of the Osterwalder-Schrader axiom of *reflection positivity* [35]. Accordingly, this propagator does not possess a Källén-Lehman spectral representation and cannot describe a physical asymptotic state. Positivity violation on the level of propagators can be tested with the help of Schwinger functions defined as

$$\Delta(t) := \frac{1}{\pi} \int_0^\infty d|p| \cos(t|p|)\sigma(p^2) \geq 0, \quad (20)$$

⁸A concise treatment can be, *e.g.*, found in refs. [6, 34].

where $\sigma(p^2)$ is a scalar function extracted from the according propagator which in case of the gluon is given by $\sigma(p^2) = Z(p^2)/p^2$ [36]. In Fig. 5 we show the Schwinger function for the gluon propagator obtained from our numerical treatment of the ghost-gluon system.

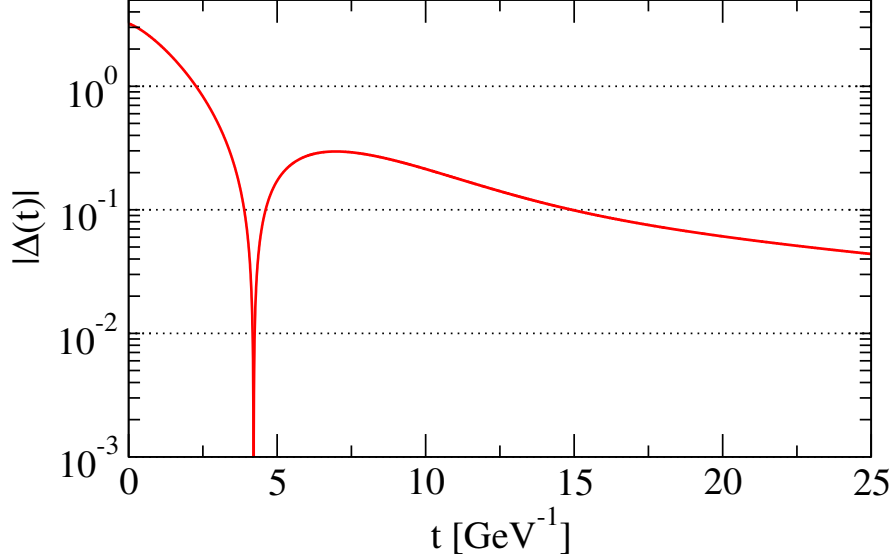


Figure 5: Displayed is the absolute value of the gluon propagator's Schwinger function on a *log – linear* plot. In accordance with [36] a zero slightly below $t = 5\text{GeV}^{-1}$ is observed which indicates the violation of positivity at a scale of roughly 1 fm.

3. Outline of the Numerical Method

The renormalized system of coupled integral equations reads

$$G(x)^{-1} = G(x_G)^{-1} + \Pi_G(x) - \Pi_G(x_G), \quad (21)$$

$$Z(x)^{-1} = Z(x_Z)^{-1} + \Pi_Z(x) - \Pi_Z(x_Z), \quad (22)$$

where $\Pi_G(x)$ and $\Pi_Z(x)$ denote the ghost and gluon self-energy terms, respectively. We now employ a Chebyshev expansion for the logarithms of the dressing functions

$$\ln G(x) = \frac{b_0}{2} + \sum_{j=1}^{N-1} b_j T_j(s(x)), \quad (23)$$

$$\ln Z(x) = \frac{a_0}{2} + \sum_{j=1}^{N-1} a_j T_j(s(x)), \quad (24)$$

where s is a suitable mapping function, which maps the $[-1, 1]$ interval of the Chebyshev polynomials to the interval $[\epsilon^2, \Lambda^2]$. We use the one proposed in [14] which reads

$$s(x) = \frac{\log_{10}(x/\Lambda\epsilon)}{\log_{10}(\Lambda/\epsilon)}. \quad (25)$$

The values for the infrared matching point and the ultraviolet cutoff used in our calculations are given by $\epsilon^2 = 10^{-6} \text{ GeV}^2$ and $\Lambda^2 = 5 \times 10^4 \text{ GeV}^2$, respectively. Expanding the logarithm of the dressing functions leads to better results in the UV regime and to a significant reduction of Chebyshev polynomials needed in the expansion [37]. Furthermore, we split the radial integration according to

$$\int_0^{\Lambda^2} \rightarrow \int_0^{\epsilon^2} + \int_{\epsilon^2}^x + \int_x^{\Lambda^2}. \quad (26)$$

In our numerical treatment the dressing functions $G(x)$ and $Z(x)$ are evaluated within the range $x \in [\epsilon^2, \Lambda^2]$. However, due to the appearance of the argument $z = x+y-2\sqrt{xy} \cos \theta \in [0, 4\Lambda^2]$ extrapolated values are required. Thus, depending on the region, a function returns the appropriate values for $G(z)$ and $Z(z)$ by taking either the numerical or the respective analytical solution. We now get a non-linear system for the Chebyshev coefficients, such that the following equations have to be fulfilled for all external momenta x

$$\begin{aligned} g(x; \mathbf{a}, \mathbf{b}) &\equiv G(x)^{-1} - G(x_G)^{-1} - \Pi_G(x) + \Pi_G(x_G) = 0, \\ z(x; \mathbf{a}, \mathbf{b}) &\equiv Z(x)^{-1} - Z(x_Z)^{-1} - \Pi_Z(x) + \Pi_Z(x_Z) = 0. \end{aligned} \quad (27)$$

Here, a vector notation for the Chebyshev coefficients is used

$$\begin{aligned} \mathbf{a} &\equiv (a_0, a_1, \dots, a_{N-1})^T, \\ \mathbf{b} &\equiv (b_0, b_1, \dots, b_{N-1})^T. \end{aligned} \quad (28)$$

In order to treat the unknown $2N$ Chebyshev coefficients, we evaluate the two equations at N external momenta⁹ x_i

$$g(x_i; \mathbf{a}, \mathbf{b}) \equiv G(x_i)^{-1} - G(x_G)^{-1} - \Pi_G(x_i) + \Pi_G(x_G) = 0, \quad (29)$$

$$z(x_i; \mathbf{a}, \mathbf{b}) \equiv Z(x_i)^{-1} - Z(x_Z)^{-1} - \Pi_Z(x_i) + \Pi_Z(x_Z) = 0. \quad (30)$$

According to [14], a Newton-Raphson method is subsequently used to linearize the system. It maps the non-linear system of equations for the Chebyshev coefficients to a linear system for the so-called Newton improvements which makes a matrix representation possible. During each iteration step new improvements are generated by a derivative of the functions z and g with respect to the $2N$ Chebyshev coefficients. These Newton improvements are then subtracted from the old coefficients in order to create a new set which is closer to the real solution, where for the initialization a starting guess is required. The two equations for the coefficients and their improvements reads

$$a_j^{n+1} = a_j^n - \varrho \Delta a_j^{n+1}, \quad (31)$$

$$b_j^{n+1} = b_j^n - \varrho \Delta b_j^{n+1}, \quad (32)$$

⁹In our calculations we use the mapped roots of the Chebyshev polynomials.

where n is the iteration step. Here, the last terms are additionally decorated with an under-relaxation parameter ρ . One advantage of the Newton method is that if the system is close enough to the real solution, the method converges quadratically. This of course depends on the starting guess. The under-relaxation parameter is used to relax the system close to the real solution also from unlucky choices of the initial conditions. After some iteration steps, this parameter can be set back to one in order to benefit from the quadratic convergence rate of the method. The Newton improvements Δa and Δb are described by a $2N \times 2N$ set of linear equations

$$\frac{\partial z^n(x_i; \mathbf{a}, \mathbf{b})}{\partial a_j} \Delta a_j^{n+1} + \frac{\partial z^n(x_i; \mathbf{a}, \mathbf{b})}{\partial b_j} \Delta b_j^{n+1} = 0, \quad (33)$$

$$\frac{\partial g^n(x_i; \mathbf{a}, \mathbf{b})}{\partial a_j} \Delta a_j^{n+1} + \frac{\partial g^n(x_i; \mathbf{a}, \mathbf{b})}{\partial b_j} \Delta b_j^{n+1} = 0. \quad (34)$$

This linear system is represented by the following matrix acting on a vector for the Δ 's

$$\begin{pmatrix} \frac{\partial z(x_0)}{\partial a_0} & \cdots & \frac{\partial z(x_0)}{\partial a_{N-1}} & \frac{\partial z(x_0)}{\partial b_0} & \cdots & \frac{\partial z(x_0)}{\partial b_{N-1}} \\ \vdots & & \vdots & \vdots & & \vdots \\ \frac{\partial z(x_{N-1})}{\partial a_0} & \cdots & \frac{\partial z(x_{N-1})}{\partial a_{N-1}} & \frac{\partial z(x_{N-1})}{\partial b_0} & \cdots & \frac{\partial z(x_{N-1})}{\partial b_{N-1}} \\ \frac{\partial g(x_0)}{\partial a_0} & \cdots & \frac{\partial g(x_0)}{\partial a_{N-1}} & \frac{\partial g(x_0)}{\partial b_0} & \cdots & \frac{\partial g(x_0)}{\partial b_{N-1}} \\ \vdots & & \vdots & \vdots & & \vdots \\ \frac{\partial g(x_{N-1})}{\partial a_0} & \cdots & \frac{\partial g(x_{N-1})}{\partial a_{N-1}} & \frac{\partial g(x_{N-1})}{\partial b_0} & \cdots & \frac{\partial g(x_{N-1})}{\partial b_{N-1}} \end{pmatrix} \begin{pmatrix} \Delta a_0 \\ \vdots \\ \Delta a_{N-1} \\ \Delta b_0 \\ \vdots \\ \Delta b_{N-1} \end{pmatrix} = \begin{pmatrix} z(x_0) \\ \vdots \\ z(x_{N-1}) \\ g(x_0) \\ \vdots \\ g(x_{N-1}) \end{pmatrix} \stackrel{!}{=} \begin{pmatrix} 0 \\ \vdots \\ 0 \\ 0 \\ \vdots \\ 0 \end{pmatrix}. \quad (35)$$

After the system iterated several times and convergence is achieved, the solutions have to vanish. Thus one needs to generate and invert the Newton matrix in order to get a new set of Newton improvements during each iteration step. A detailed description on the implementation of the numerical method outlined above will be given after some general remarks on GPU programming.

4. GPU Calculations using CUDATM

During the last years, programmable Graphic Processor Units (GPUs) became more and more important in scientific and engineering high performance computing. Due to their multi-threaded manycore processor architecture, they are perfectly well-suited in dealing with compute-intensive, parallel programs. There are several programming models available like OpenCLTM or DirectComputeTM for instance. We use CUDATM for the numerical implementation of our problem, the parallel computing model provided by NVIDIA[®].

4.1. Kernels, Blocks and Threads

A CUDATM code runs on the host CPU as a serial program in which the compute intensive parts are condensed into one or more kernel functions to be performed in parallel on the GPU device. In order to be scalable, the kernels are structured into a three-level hierarchy of threads. The top level is represented by a grid of thread-blocks with up to 1024 threads acting within one block. Thread-blocks represent the second hierarchy level and contain the same number of threads in each case. A single thread stands at the lowest hierarchy level and represents the basic building block of a kernel function. The distribution of thread-blocks to the different device multiprocessors is managed by the hardware and there is no possibility to decide which block is performed on which multiprocessor at a given time. For that reason, blocks have to be independent from each other.

A single multiprocessor which operates on a specific block executes several threads in parallel, grouped to a so-called warp. The individual threads in a warp have the same start address in the program but can act on/with different data and are in principle free to branch and follow different execution paths. In this case each branch path is executed sequentially (warp divergence), where at the end the threads converge back to the original execution path and the multiprocessor can handle the next warp. Warp divergence has a considerable effect on the run time of the program and best performance is achieved if all threads of a warp agree on their particular execution path.

Each multiprocessor owns a specific number of registers. These memory spaces are dynamically assigned to the corresponding threads currently running on the multiprocessor. Whereas each thread can operate on its specific register space, there is also the possibility that threads within a block can interchange data via a very fast shared memory. Communication between different blocks in a grid can only occur via a global memory space which is slower than the shared memory. The global memory can be accessed by all the threads within the kernels as well as by the host to read/write the corresponding data. Although global memory access is still roughly ten times faster than the main memory access of a conventional CPU, it is favorable to minimize the communication of threads with the global memory during a kernel call. If the memory access is not performed in a coalesce way [38, 39] it can be that some threads already operate on their specific data while others have to wait for data arriving from the global memory.

In general the optimization of a CUDATM program benefits from several tasks. First the communication between the host and the device as well as out-of-order accesses to the global memory from kernels have to be minimized. Furthermore, the overall performance of the program also depends on the number of blocks and the blocksize. Running only one block per multiprocessor can force the specific processor to idle because of latencies in memory access and/or block synchronization. Launching several blocks decreases register and shared memory resources available to a single thread-block. The blocksize strongly depends on the workload each thread has to perform and on the number of registers available per block. It can very well happen that the possible number of threads is below the maximal number of threads given in the device specifications simply because of the heavy register usage of compute intensive threads.

4.2. Implementation on a Graphics Device with CUDATM

The central task of the code is to generate the Jacobian matrix for the Newton improvements. Therefore we split the matrix into sub-matrices which are distributed onto four different kernel functions

$$\mathcal{J} = \begin{pmatrix} \frac{\partial z(x_0)}{\partial a_0} & \cdots & \frac{\partial z(x_0)}{\partial a_{N-1}} & \frac{\partial z(x_0)}{\partial b_0} & \cdots & \frac{\partial z(x_0)}{\partial b_{N-1}} \\ \vdots & \text{Kernel 1} & \vdots & \vdots & \text{Kernel 2} & \vdots \\ \frac{\partial z(x_{N-1})}{\partial a_0} & \cdots & \frac{\partial z(x_{N-1})}{\partial a_{N-1}} & \frac{\partial z(x_{N-1})}{\partial b_0} & \cdots & \frac{\partial z(x_{N-1})}{\partial b_{N-1}} \\ \frac{\partial g(x_0)}{\partial a_0} & \cdots & \frac{\partial g(x_0)}{\partial a_{N-1}} & \frac{\partial g(x_0)}{\partial b_0} & \cdots & \frac{\partial g(x_0)}{\partial b_{N-1}} \\ \vdots & \text{Kernel 3} & \vdots & \vdots & \text{Kernel 4} & \vdots \\ \frac{\partial g(x_{N-1})}{\partial a_0} & \cdots & \frac{\partial g(x_{N-1})}{\partial a_{N-1}} & \frac{\partial g(x_{N-1})}{\partial b_0} & \cdots & \frac{\partial g(x_{N-1})}{\partial b_{N-1}} \end{pmatrix}. \quad (36)$$

These kernels can now be launched on the available GPU devices. Once the matrix elements are derived, a data transfer to the host takes place where the inversion of the matrix is performed. As the size of the matrix is rather small, the inversion can be done with standard LU decomposition routines on the host. The time usage of this procedure is negligible compared to the generation of the matrix. On the particular device the sub-matrix is split into blocks of size N

$$\begin{pmatrix} \frac{\partial z(x_0)}{\partial a_0} & \frac{\partial z(x_0)}{\partial a_1} & \cdots & \frac{\partial z(x_0)}{\partial a_{N-1}} \\ \frac{\partial z(x_1)}{\partial a_0} & \frac{\partial z(x_1)}{\partial a_1} & \cdots & \frac{\partial z(x_1)}{\partial a_{N-1}} \\ \vdots & \vdots & \text{GPU1} & \vdots \\ \frac{\partial z(x_{N-1})}{\partial a_0} & \frac{\partial z(x_{N-1})}{\partial a_1} & \cdots & \frac{\partial z(x_{N-1})}{\partial a_{N-1}} \end{pmatrix}. \quad (37)$$

$\begin{matrix} \uparrow & \uparrow & & \uparrow \\ \text{Block 1} & \text{Block 2} & \dots & \text{Block N} \end{matrix}$

These blocks are completely independent, *i.e.*, no data transfer or communication with the host or between the threads in the block is needed. In addition, the derivatives can be performed by two threads

$$\frac{\partial z(x_i)}{\partial a_j} = \frac{z(x_i; \mathbf{a}|_{a_j+\epsilon_j}, \mathbf{b}) - z(x_i; \mathbf{a}|_{a_j-\epsilon_j}, \mathbf{b})}{2\epsilon_j}, \quad (38)$$

where finally one of the two threads has to sum up and divide the result by $2\epsilon_j$. In our numerical simulation we use $\epsilon_j \approx 10^{-5}a_j$ as the derivatives are symmetric. Note that in

each block the same derivatives are used such that the corresponding vectors can be pre-calculated in parallel during each iteration step and stored as an array which is, in case of the matrix part treated in Eq. (38), of the form

$$\begin{pmatrix} a_0 + \epsilon_0 & a_0 & \dots & a_0 \\ a_1 & a_1 + \epsilon_1 & \dots & a_1 \\ \vdots & \vdots & \ddots & \vdots \\ a_{N-1} & a_{N-1} & \dots & a_{N-1} + \epsilon_{N-1} \\ \hline a_0 - \epsilon_0 & a_0 & \dots & a_0 \\ a_1 & a_1 - \epsilon_1 & \dots & a_1 \\ \vdots & \vdots & \ddots & \vdots \\ a_{N-1} & a_{N-1} & \dots & a_{N-1} - \epsilon_{N-1} \end{pmatrix}. \quad (39)$$

These arrays are generated on the GPU devices according to their assigned sub-matrix. Subsequently, the blocks can load their specific derivative vector into the shared memory with respect to their block and thread IDs. Our code is separated into an initialization part running on the host and a main part which is performing the generation of the Newton matrix. The first part deals with the memory management, the initialization of the Chebyshev coefficients as well as the transfer of the corresponding data to the different devices. Note that the weights and nodes for the quadratures, which are generated on the host, are stored within the constant memory of the devices. The main part is split up into four kernel functions for the four different domains of the Newton matrix as well as one kernel function for the generation of the solutions vector. These kernels are launched in parallel on the specific devices using the *cudaSetDevice* instruction. In our numerical implementation using OpenMPI each process invokes a GPU device according to its specific process ID¹⁰. After the kernels generated their particular part of the matrix a data transfer to the host is performed where the LU decomposition/substitution takes place. The generation of the derivatives is performed in parallel by an additional kernel in the beginning of each iteration step. In the following we show performance results of the serial code and compare with a parallelized version using OpenMPI as well as CUDATM.

¹⁰We note that the usage of a separate GPU device for the generation of the solutions vector is less efficient. As this step requires an additional compute node, the benefits of the additional resources are most probably spoiled by the expensive communication paths between the two machines as there are only four GPU devices per machine. Here, the overall performance of the code is improved if one of the four MPI processes, in our case the master process, performs the calculation of the solutions vector as well as one ghost part of the matrix. The master process collects the data from the other MPI processes via a *MPI.Gather* operation such that in this setting no data transfer is needed. We note that using this configuration also three GPUs would be enough, as the run time of the two processes performing the ghost parts is comparable to the run time of a single process performing one gluon part of the matrix. Nevertheless, the following performance tests were carried out on four GPUs.

5. Performance Results

We tested various versions of the numerical method outlined in Sec. 3. The easiest approach is to perform the calculations on a single CPU device¹¹. Subsequently, we parallelized the code using OpenMPI which is, due to the nature of the problem, a straightforward task. Each element of a Newton sub-matrix is generated in blocks according to the number of processes launched, starting from the top left entry. Here, only the master process has to allocate memory for the whole matrix since the other processes are calculating just the elements. Since the communication load is negligible, this procedure scales quite well with the number of processors available. The final step is the GPU implementation, where we additionally compare a single and a multi GPU version¹².

For the numerical calculations the following hardware is used:

- Intel Core2 Quad Processor Q9400 @ 2.66GHz (no Hyper-Threading capabilities),
- Intel Xeon Six-Core X5650 @ 2.67GHz,
- NVIDIA Geforce GTX 560 Ti 448 Cores,
- NVIDIA Tesla C2070.

The Xeons are additionally connected via 40Gb/s QDR InfiniBand, whereas for the Core2s a standard Gigabit-Ethernet LAN is used. The following table shows performance results obtained on the specific hardware using the different numerical implementations, where the value in brackets denotes the number of cores/devices used for the corresponding calculation. By varying the number of radial integration nodes and Chebyshev polynomials, six different work-loads are employed.

Nodes	Q(1)	Q(12)	Xe(1)	Xe(12)	GTX(1)	Tesla(1)	Tesla(4)	Speed-up
32	1.63	0.14	3.75	0.42	0.08	0.07	0.04	94/11
64	3.27	0.29	7.34	0.86	0.13	0.11	0.06	122/14
64	14.80	1.30	23.45	2.05	0.27	0.23	0.10	235/21
128	29.58	2.58	48.38	4.25	0.53	0.45	0.15	323/28
64	54.32	4.70	74.22	6.40	0.58	0.40	0.15	495/43
128	119.33	9.39	152.05	13.08	1.15	0.75	0.27	563/48

Table 1: The run time of the code in minutes using 36/60/96 Chebyshev polynomials (upper/middle/lower part of the table) for each dressing function. For the radial integral 32/64/128 Gauss-Legendre nodes are employed within each of the three integration intervals, cf. eq. (26).

¹¹The numerical problem discussed here can be solved quite fast on a single CPU, see table 1. The current (described) calculations provided in table 1 serve, however, as an important test case because in the near future much more involved truncation schemes of DSEs will be investigated.

¹²For an accurate performance test we use rather large workloads and we furthermore employ the fit functions proposed in [16] to initiate the system setting the under-relaxation parameter $\varrho = 1$ in this case. Using this setup the system iterates four times, where we implemented a cross sum check over all Chebyshev coefficients with an epsilon of $\epsilon = 10^{-6}$.

The upper/middle/lower part of Tab. 1 represents the performance test using 36/60/96 Chebyshev polynomials for each dressing function, where the entries denote the run time of the code in minutes. Here, the approximate speed-ups are measured between the slowest and the fastest implementation on the one hand (first number) and within a more equitable setup by comparing twelve Xeons with four Teslas (second number). With increasing workload, the GPUs perform successively better and we would like to emphasize that already with the relatively low-priced consumer card impressive speed-ups can be obtained. In Fig. 6 we show the scaling of the MPI code when the number of CPU cores is increased (for both the Core2s and the Xeons). Here 128 radial integration points are used within each integration region as well as 48 Chebyshev polynomials for each dressing function.

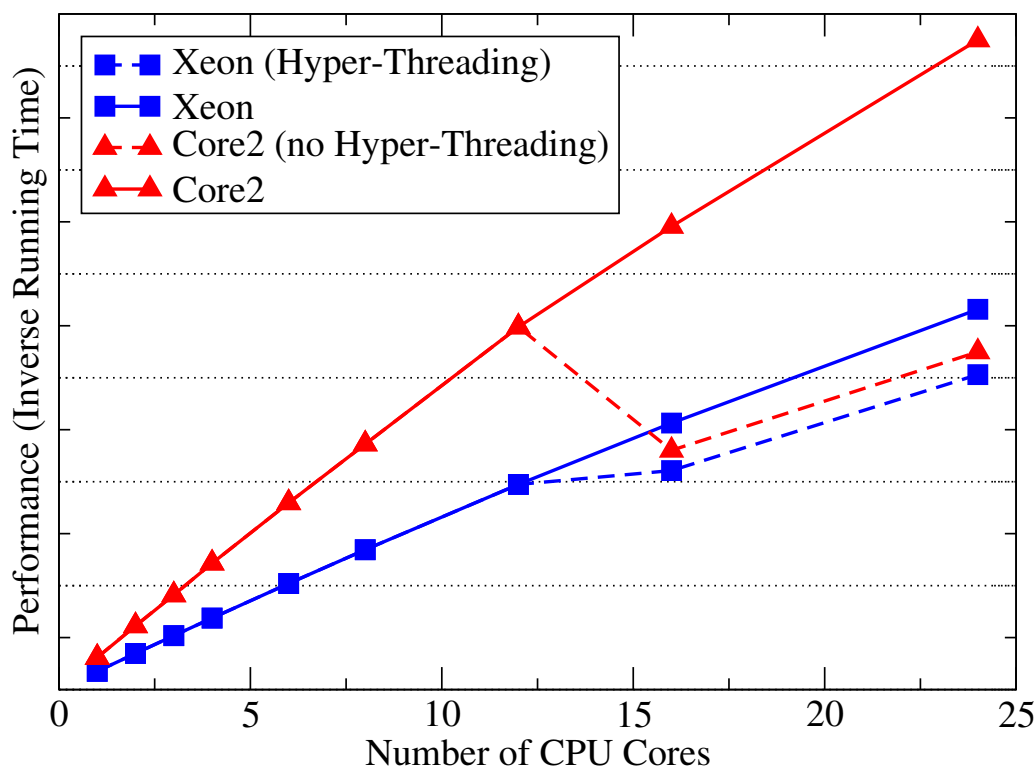


Figure 6: The expected linear performance gain of the MPI code when the number of CPU cores is increased (solid lines). Whereas in a direct comparison of the two architectures the Xeons are slower, Intel’s Hyper-Threading technology increases the efficiency of the server CPUs by approximately 40% (blue dashed line). Here, 16/24 threads are launched on twelve CPU cores. The Core2s show a considerable performance break down in this case since Hyper-Threading is not available on these devices (red dashed line).

Both measurements show the expected linear scaling behavior (solid lines). Launching more processes than CPU cores available (dashed lines) results in a serious performance drop of the Core2s. Due to Intel’s Hyper-Threading technology, a single Xeon core can operate on two threads concurrently which results in a performance loss of only 20% compared to a test run using the corresponding number of real cores. In Fig. 7 the blocksize dependence of the CUDATM code for the two different types of GPUs is shown.

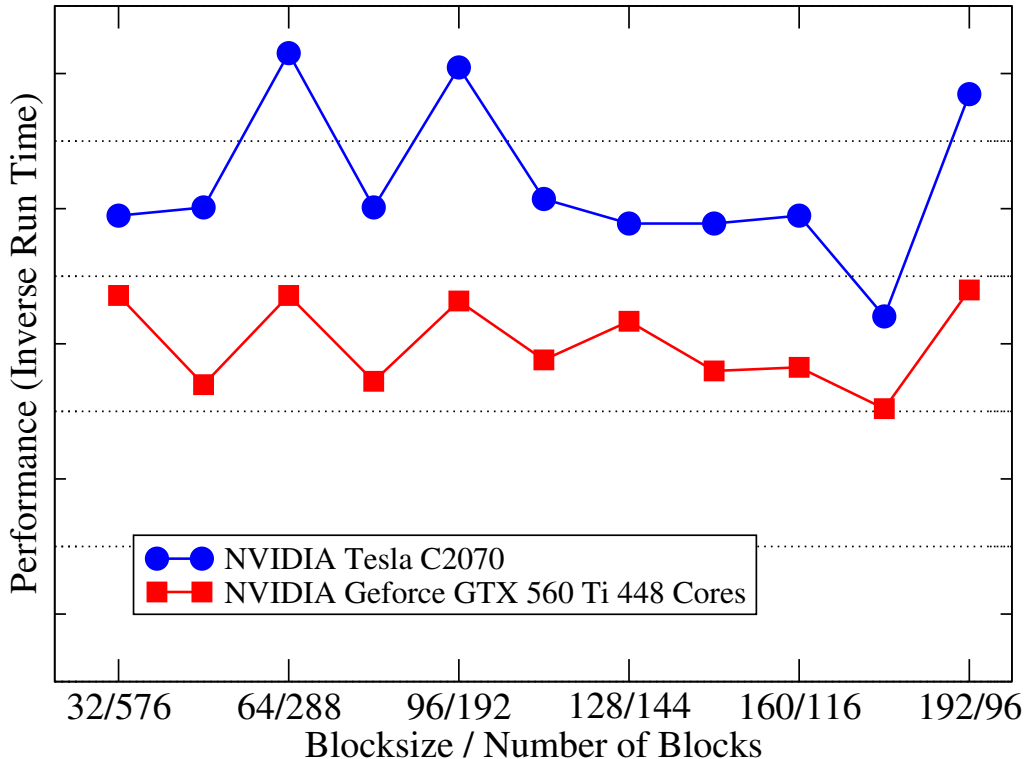


Figure 7: The impact of the blocksize on the performance for test runs on single GPUs using 96 Chebyshev polynomials and 128 radial integration points. The axes label denotes the blocksize and the number of blocks, respectively (note that two threads are performing a single matrix entry as mentioned in Sec. 4). One can see some slight deviations in the overall behavior of the different types of GPUs but in any case choosing the blocksize to be a multiple of a warp leads to optimal performance. Furthermore, these effects become noticeable only for rather large workloads. Thus, a blocksize equal to the number of Chebyshev polynomials (and equal to a multiple of a warp) is a convenient choice for almost all practical calculations.

Let us finally comment on the calculation of the Schwinger function. The integral in eq. (20) is easily implemented on a GPU device since it is a generalized scalar product and can be treated using standard techniques [38]. The kernels are decomposed into a one-dimensional grid of thread-blocks for the Euclidean time steps δt , where we used strides [39] to reduce the results in the end. However, the main improvements can be obtained from a parallelized generation of the nodes and weights. For the computation a (mapped) Gauss-Legendre quadrature rule is used. The following table shows performance results where the entries denote the run time in seconds¹³.

¹³Here, the speed-ups are measured between the GPUs and the Xeons and we used 2^{17} Gauss-Legendre nodes. Also in this case an OpenMPI version is possible in principle. However, the usage of multiple GPUs is not reasonable due to the reduced complexity of this problem.

	Q(1)	Xe(1)	GTX(1)	Tesla(1)
sequential	213.5	226.9		
CUDA TM			4.1	3.9
speed-up			55	58

Table 2: Performance results for an evaluation of the integral in eq. (20).

6. Conclusions

We performed a numerical analysis of the ghost-gluon Dyson-Schwinger equations (DSEs) of Yang-Mills theory. The truncated system of non-linear integral equations was solved with the help of a Chebyshev expansion for the dressing functions using subsequently a Newton-Raphson method to obtain a linear system. Here, the methods are ideally suited for an SIMD architecture as the problem decomposes into independent parts. The parallelization of the system was performed using OpenMPI and CUDATM. By comparing the two parallelization strategies we demonstrated the computational advantage of GPUs for this problem. Compared to a sequential version we obtained speed-ups of approximately two orders of magnitude already with a single consumer GPU. The presented results demonstrate convincingly the benefits of modern GPU devices in DSE calculations, and the proposed solution strategy offers a helpful toolbox.

Last but not least, the generalization to larger systems is straightforward since additional DSEs can be incorporated by extending the Newton matrix with the corresponding derivatives. In this respect we provided a basis for on-going and future computations which uses the Yang-Mills DSE system as input. Here, the GPU version does and is expected to perform successively better with increasing workload.

Acknowledgements

We thank Markus Q. Huber and Manfred Liebmann for valuable discussions. This work was supported by the *Research Core Area "Modeling and Simulation"* of the Karl-Franzens University Graz and by the Austrian Science Fund (FWF DK W1203-N16).

References

- [1] F. J. Dyson, Phys. Rev. **75** (1949) 1736.
- [2] J. S. Schwinger, Proc. Nat. Acad. Sc. **37** (1951) 452; *ibid.*, 455.
- [3] R. Alkofer and L. von Smekal, Phys. Rept. **353** (2001) 281 [arXiv:hep-ph/0007355].
- [4] P. Maris and C.D. Roberts, Int. J.Mod. Phys. E**12** (2003) 297 [arXiv:nucl-th/0301049].
- [5] C. S. Fischer, J. Phys. G **32** (2006) R253 [arXiv:hep-ph/0605173].

- [6] R. Haag, “Local quantum physics: Fields, particles, algebras,” Berlin, Germany: Springer (1992) 356 p. (Texts and monographs in physics)
- [7] L. von Smekal, R. Alkofer and A. Hauck, Phys. Rev. Lett. **79** 3591 (1997) 3591 [arXiv:hep-ph/9705242]; L. von Smekal, A. Hauck and R. Alkofer, Annals Phys. **267** (1998) 1 [Erratum-ibid. **269** (1998) 182] [arXiv:hep-ph/9707327].
- [8] D. Zwanziger, Phys. Rev. D **65** (2002) 094039 [arXiv:hep-th/0109224].
- [9] C. Lerche and L. von Smekal, Phys. Rev. D **65** (2002) 125006 [arXiv:hep-ph/0202194].
- [10] R. Alkofer, C. S. Fischer and F. J. Llanes-Estrada, Phys. Lett. B **611** (2005) 279 [arXiv:hep-th/0412330]; M. Q. Huber, R. Alkofer, C. S. Fischer and K. Schwenzer, Phys. Lett. B **659** (2008) 434 [arXiv:0705.3809 [hep-ph]].
- [11] C. S. Fischer and J. M. Pawłowski, Phys. Rev. D **80** (2009) 025023 [arXiv:0903.2193 [hep-th]].
- [12] L. Fister, R. Alkofer and K. Schwenzer, Phys. Lett. B **688** (2010) 237 [arXiv:1003.1668 [hep-th]].
- [13] S. Mandelstam, Phys. Rev. D **20** (1979) 3223.
- [14] D. Atkinson and J. C. R. Bloch, Phys. Rev. D **58** (1998) 094036 [hep-ph/9712459].
- [15] P. Watson and R. Alkofer, Phys. Rev. Lett. **86** (2001) 5239 [arXiv:hep-ph/0102332].
- [16] C. S. Fischer, Ph.D. thesis, Tübingen University, 2003; [arXiv:hep-ph/0304233].
- [17] A. C. Aguilar, D. Binosi and J. Papavassiliou, Phys. Rev. D **78** (2008) 025010 [arXiv:0802.1870 [hep-ph]].
- [18] P. Boucaud *et al.*, JHEP **0806** (2008) 099 [arXiv:0803.2161 [hep-ph]].
- [19] C. S. Fischer, A. Maas and J. M. Pawłowski, Annals Phys. **324** (2009) 2408 [arXiv:0810.1987 [hep-ph]].
- [20] A. Cucchieri and T. Mendes, PoS LATTICE **2010** (2010) 280 [arXiv:1101.4537 [hep-lat]].
- [21] A. Maas, arXiv:1106.3942 [hep-ph].
- [22] J. M. Pawłowski, D. F. Litim, S. Nedelko and L. von Smekal, Phys. Rev. Lett. **93**(2004) 152002 [arXiv:hep-th/0312324].
- [23] T. Kugo and I. Ojima, Prog. Theor. Phys. Suppl. **66** (1979) 1.
- [24] N. Nakanishi and I. Ojima, World Sci. Lect. Notes Phys. **27** (1990) 1.

- [25] V. N. Gribov, Nucl. Phys. B **139** (1978) 1.
- [26] D. Zwanziger, Nucl. Phys. B **364** (1991) 127; Nucl. Phys. B **399** (1993) 477.
- [27] A. Sternbeck and L. von Smekal, Eur. Phys. J. C **68**, 487 (2010) [arXiv:0811.4300 [hep-lat]].
- [28] A. Maas, Phys. Lett. B **689** (2010) 107 [arXiv:0907.5185 [hep-lat]].
- [29] A. Maas, J. M. Pawłowski, D. Spielmann, A. Sternbeck and L. von Smekal, Eur. Phys. J. C **68** (2010) 183 [arXiv:0912.4203 [hep-lat]].
- [30] J. C. Taylor, Nucl. Phys. B **33** (1971) 436.
- [31] H. Takahasi and M. Mori, Publications of the Research Institute for Mathematical Sciences **9** (1974) 721.
- [32] C. S. Fischer and M. R. Pennington, Phys. Rev. D **73** (2006) 034029 [hep-ph/0512233].
- [33] A. Sternbeck, E. -M. Ilgenfritz, M. Müller-Preussker and A. Schiller, Phys. Rev. D **72** (2005) 014507 [arXiv:hep-lat/0506007].
- [34] J. Glimm and A. M. Jaffe, “Quantum Physics. A Functional Integral Point Of View,” New York, Springer (1987) 535p
- [35] K. Osterwalder and R. Schrader, Commun. Math. Phys. **31** (1973) 83; Commun. Math. Phys. **42** (1975) 281.
- [36] R. Alkofer, W. Detmold, C. S. Fischer, P. Maris, Phys. Rev. **D70** (2004) 014014 [hep-ph/0309077]; Nucl. Phys. Proc. Suppl. **141** (2005) 122 [arXiv:hep-ph/0309078].
- [37] A. Maas, Comput. Phys. Commun. **175** (2006) 167 [arXiv:hep-ph/0504110].
- [38] NVIDIA Corporation, CUDA Programming Guide 4.2 (2012).
- [39] NVIDIA Corporation, CUDA Design Guide 4.1 (2012).